Crystallisation rates of calcite from an amorphous precursor in confinement

Robert Darkins[a], Alexander S. Côté[a], Colin L. Freeman[b], Dorothy M. Duffy[a,*]

[a] *Department of Physics and Astronomy, University College London, Gower Street, London, WC1E 6BT (UK)*
[b] *Department of Materials Science and Engineering, University of Sheffield, Sheffield, S1 3JD (UK)*

Abstract

Using molecular dynamics, we simulate the crystallisation of calcite from an amorphous calcium carbonate precursor within the confines of a cylindrical potential. The crystallisation rates of various low-index calcite surfaces are measured. A notable inhibition in the growth of the (00.1) surface is observed and a mechanism relating to the rotation of the carbonate ions is proposed to explain it.

Keywords: A1. Biocrystallisation, B. Calcium carbonate, B. Calcite, A1. Growth rates, A2. Growth from melt

1. Introduction

Calcium carbonate ($CaCO_3$) is one of the most important and abundant biominerals on earth and crystallises into one of three polymorphs: calcite (the most stable), aragonite and vaterite. Amorphous calcium carbonate (ACC) is also recognised as a common biomineral that exists in both anhy-

*Corresponding author. E-mail address: d.duffy@ucl.ac.uk

drous and hydrated forms [1]. The transient anhydrous ACC phase occurs as a precursor to the crystalline polymorphs and is commonly exploited by biological systems; rather than precipitate directly from solution, biogenic single crystals grow from an amorphous precursor that has precipitated within a constrained volume, such as a vesicle or a cellular membrane [2]. This strategy enhances the chemical and structural control that biological systems have over mineralisation. For instance, the local mineralisation site can act as a mould, bestowing a particular morphology upon the amorphous precursor which is retained post-crystallisation. The tri-radiate spicules of sea urchin larvae provide a well-studied example of this [3, 4]. Furthermore, crystallising directly from a dense precursor circumvents the slow ion diffusion characteristic of classical growth, and facilitates the use of additives in further controlling growth [5].

Track-etched membranes were identified by Loste and Meldrum [6] to be an ideal system for studying the crystallisation of calcite from ACC in confinement and have since been applied in other studies [7, 8]. These experiments involve precipitating amorphous calcium carbonate within cylindrical pores etched into a polycarbonate membrane, with diameters ranging from 50 nm to 10 μm depending on the study. The ACC subsequently crystallises to form single crystals of calcite with cylindrical morphologies.

Inspired by this experimental work, we have employed molecular dynamics to model the crystallisation of calcite from anhydrous ACC *in vacuo* within the confines of a cylindrical potential well. The crystallisation rate was enhanced by imposing an elevated temperature of 1000 K, in contrast to previous simulations of ACC that employed metadynamics to enhance the

crystallisation rate [9, 10, 11]. Such a temperature is unrealistically high but we would expect the same growth mechanisms to dominate at room temperature. We report the relative growth rates of six low-index surfaces and present a comparison of the structural evolution of the two polar surfaces.

Water is known to play a significant role in the crystallisation of calcium carbonate [12] and its absence from our model may appear to be a crucial factor. However, transient ACC is usually anhydrous and is often isolated from solution in nature. Indeed, Beniash et al. [13] suggest that organisms may expel water in order to increase control over crystallisation. There is also strong evidence from biogenic systems that dehydration of ACC precedes its crystallisation even in aqueous environments [14].

It will also be seen that our model induces a solid-state ACC-to-calcite transformation as opposed to the dissolution-reprecipitation mechanism observed in, e.g., Ref [7]. The prevalence of such a transformation has yet to be established experimentally but it has been inferred to have occurred both *in vivo* [3, 13, 15] and *in vitro* [16, 17].

2. Methodology

2.1. The molecular dynamics model

The confining role of the pores in the track-etched membrane was emulated by an external cylindrical potential of the form

$$V_{\text{ext}}(x, y, z) = \left(3\,\text{nm} - \sqrt{x^2 + y^2}\right)^{-6} \text{J/mol}. \tag{1}$$

A calcite crystal consisting of 3190 $CaCO_3$ units was melted at 3000 K within this cavity so as to acquire ACC. This is a standard method for

producing ACC in MD studies of calcium carbonate. The ACC adopted the same cylindrical morphology of the potential, assuming a diameter and length of approximately 5 nm and 12 nm, respectively.

After melting, a calcite cylinder was added to one end of the amorphous rod. The calcite cylinder was frozen while the remaining system was quenched at 1000 K. At this temperature the ACC was metastable with respect to the calcite cylinder which acted as a nucleus for the subsequent calcite growth within the ACC. The growth surface could be selected by constructing our artificial nucleus to have the desired crystal orientation. This model is illustrated in Figure 1.

The MD simulations were carried out using the `DL_POLY Classic` [18] software package in the canonical (NVT) ensemble. Rhombohedral periodic boundary conditions ($6 \times 6 \times 18$ nm) were imposed so that the Ewald summation method could be employed to handle the long-range electrostatics; a vacuum slab of approximately 5 nm prevented self-interaction between the images. The calcium carbonate was described by the Pavese [19] interatomic potential. The pressure was zero. The Nosé-Hoover thermostat was used to maintain the desired temperature. The Verlet algorithm with a time-step of 1 fs was used to integrate the equations of motion.

2.2. Measuring the crystallisation rate

The first step in our method for measuring the crystallisation rate was the identification of a suitable subset of the rod for the analysis. This subset, of cross-sectional area A, was chosen to enclose only the bulk of the rod, as illustrated in Figure 1. The bulk is only used as identifying order within the surface is unreliable and also the cross-sectional area is required

in computing the crystallisation rate, as detailed below. The next step was the computation of the function $n(t)$ which counts the number of ions within the subset that belong to the calcite grain at time t. Measuring this quantity involves distinguishing ions with a local crystal structure from those with no crystal structure. To achieve this, Steinhardt et al [20] introduced the following complex numbers that quantify the local order of each particle j,

$$q_{\ell m}(j) = \frac{1}{n_b(j)} \sum_{k \in \text{bonded}} Y_\ell^m(\mathbf{r}_{jk}), \qquad -\ell \leq m \leq \ell \tag{2}$$

where $n_b(j)$ equals the number of particles bonded to particle j, $Y_\ell^m(\mathbf{r})$ are the spherical harmonics of degree ℓ in the direction $\mathbf{r}$, and $\mathbf{r}_{jk}$ is the vector connecting particle j to particle k. We define particle k as being *bonded* to particle j if it falls within the first neighbour shell (from the pair correlation function, $r_{jk} < 3.6$ Å). These complex numbers can be combined into a rotationally-invariant form,

$$q_\ell(j) = \left[\frac{4\pi}{2\ell + 1} \sum_{m=-\ell}^{\ell} |q_{\ell m}(j)|^2 \right]^{1/2} \in [0, 1], \tag{3}$$

which provides a sort of "shape spectroscopy" for an appropriately chosen ℓ, whereby $q_\ell(j)$ assumes a value that reflects the local crystal symmetry of particle j.

Lechner and Dellago [21] proposed that the $q_{\ell m}(j)$ parameters be averaged over the first neighbour shell and the particle j itself, resulting in the new parameter

$$p_{\ell m}(j) = \frac{1}{n_b(j) + 1} \left[q_{\ell m}(j) + \sum_{k \in \text{bonded}} q_{\ell m}(k) \right], \tag{4}$$

which can be combined to form the rotationally-invariant $p_\ell(j)$ in a way

analagous to Eq. (3). This modification was shown to achieve a higher sensitivity to differing structures.

The q_ℓ order parameters have been applied to calcium carbonate in previous work; in Refs [11, 22] they were employed to characterise all three of the crystalline polymorphs (at room temperature and atmospheric pressure). Delineating multiple polymorphs requires that q_ℓ be evaluated between various pairs of species, C-C, C-Ca, Ca-O, etc. In this work, however, we are forcing the calcite polymorph only and so have the convenience of treating all calcium and carbonate ions as single particles of an indistinguishable species.

Four order parameters, q_4, p_4, q_6 and p_6, were sampled to find the most effective at differentiating calcite from ACC. The effectiveness of each can be gauged by computing their distribution in a sample of bulk calcite and, separately, in a sample of bulk ACC. At 1000 K these distributions will inevitably overlap since the high temperature blurs the division between the two phases; the objective is to minimise the overlap. The distributions of the four order parameters are plotted in Figure 2 where it can be seen that p_4 has the least overlap, with the calcite and ACC distributions delimited by the value $p_4 = 0.53$. We therefore define the function $n(t)$ to be the number of ions j in the subset at time t that satisfy

$$p_4(j) > 0.53. \tag{5}$$

The gradient dn/dt, obtained through linear regression, measures the average rate at which the calcite grain grows. The crystallisation rate, defined to be the rate of layer formation, is then simply the gradient dn/dt divided

by the number of ions per layer,

$$G = \frac{1}{\rho A}\frac{dn}{dt}, \tag{6}$$

where ρ is the ionic density for the surface orientation of interest (listed in Table 1).

3. Results and discussion

3.1. Relative crystallisation rates

The crystallisation rates of six surfaces were measured using the approach outlined above and are presented in Table 1. The function $n(t)$ for each surface is plotted in Figure 3 and reveals steady growth in all cases with the exception of (01.8), discussed in §3.2.

It is informative to compare our observed growth rates to those predicted by crystal growth models, focusing on those that predict the growth morphology as opposed to the equilibrium morphology based on surface energies [23]. In particular, the Bravais-Friedel-Donnay-Harker (BFDH) law [24, 25, 26] states that the most important crystallographic forms will have the greatest interplanar spacings. Consequently, as a rule of thumb, surfaces with lower ionic densities ρ are expected to crystallise quicker. From the values of ρ presented in Table 1, it can be seen that the non-polar orientations, (10.0), (01.8), (11.0), and (10.4), do indeed crystallise with the relative order predicted by BFDH. The polar orientations, on the other hand, both fall short of their predicted ranks: (01.2) by only one place but (00.1) by a significant amount.

Growth models based on attachment energies [27] appear congruous with BFDH. The attachment energies for a subset of the surfaces considered in

this work were computed in Ref [28] for unrelaxed surfaces using the same interatomic potential employed here. The non-polar surfaces for which the data is available are found to crystallise in the order predicted based on these attachment energies, E_{attach}, presented in Table 1. The polar (00.1) surface, however, remains significantly slower than expected. The cause of this inhibition will be discussed in §3.3.

It should be noted that we reproduced the relative order of the growth rates presented in Table 1 for slabs periodic in two dimensions. The results are therefore not unique to confined systems.

3.2. The (01.8) *surface*

The growth of the nanorod with the (01.8) nucleus is noteworthy. In constrast to the other orientations, this particular rod initially grew a few layers with the desired (01.8) surface but then other growth surfaces emerged. Visual inspection revealed a pair of {10.4} planes that met in the centre of the rod and were intersected by a {00.1} plane from a perpendicular direction, see Figure 4. The transition from the flat (01.8) surface to this hybrid surface is apparent in the plot of $n(t)$ in Figure 3 where the growth rate is seen to drop off quite significantly after an initially high rate. The resultant growth surface persisted throughout the crystallisation of the rod, supporting our claim that (00.1) and (10.4) are both notably (and equally) slow surfaces.

The measured growth rate for (01.8) that is presented in Table 1 is based only on the growth of the first few layers. As the secondary growth front emerged, the growth rate dropped off by a factor of five.

3.3. The polar surfaces

Both of the polar surfaces, (00.1) and (01.2), were found to grow slower than theoretically predicted. This inhibition may be attributable to the layering process which is slightly more involved in the polar surfaces since it involves charge separation. It is also plausible that the crystallisation of polar surfaces entails a greater level of cooperation between consecutive layers than it does in the non-polar surfaces and that this further impedes growth. It is not so clear, however, why the (00.1) surface should grow significantly (30%) slower than (01.2) despite being significantly (40%) less dense.

Crystallisation of polar surfaces involves two slightly overlapping stages: the separation of charge into layers, followed by the ionic ordering within those layers. In both polar surfaces, the charge was observed to separate rapidly near to the crystal surface and the rate-limiting step was found to be the ionic ordering. To demonstrate this, let us define $\mathbf{n}_j$ to be the unit vector normal to the carbonate j that has a non-negative z component. We then introduce the following order parameter for the kth layer of carbonate ions,

$$\sigma_k = \sqrt{\langle (\cos^{-1} |\mathbf{n}_j \cdot \langle \mathbf{n}_j \rangle_j^k|)^2 \rangle_j^k}, \tag{7}$$

where $\langle \cdot \rangle_j^k$ denotes the average over all carbonates j belonging to the kth crystal layer. By tracing all of the carbonate ions belonging to the kth layer through time, this quantity provides a measure of how unified their directions are (and therefore how ordered the layer is) at each moment in time, ranging from ~ 0.9 rad in the case of ACC to ~ 0.2 rad in the case of the final calcite layer. Plotting this parameter for the (arbitrarily chosen) second carbonate layer in each rod (Figure 5a) reveals that the ions order more rapidly in

(01.2), from which we conclude that the ionic ordering is indeed the source of inhibition for (00.1). We now consider the cause of this.

The direction of each carbonate can be represented in (hemi)spherical coordinates (θ, ϕ), where $\phi \in [0, 90°]$ is the angle between the normal of the carbonate and the growth direction, and $\theta \in [0, 360°)$ is the corresponding azimuthal angle. In amorphous calcium carbonate, the orientations of the carbonates are randomly distributed and so the probability of finding a carbonate aligned within the differential solid angle $d\Omega(\theta, \phi) \equiv \sin(\phi)\, d\phi\, d\theta$ will be directly proportional to $d\Omega \propto \sin(\phi)$. It follows that carbonate ions with a larger ϕ will be more abundant in ACC than those with a smaller ϕ. The carbonate ions in the (01.2) surface have a fairly large ϕ angle of 63°, compared with $\phi = 0°$ for the (00.1) surface. Consequently, as noted in [29], the ϕ-distribution in ACC has a much closer resemblance to that in (01.2). This can be seen to be the case in Figures 5b and 5c where the ϕ-distribution of the second carbonate layer is plotted for both (01.2) and (00.1) at the three stages labelled in Figure 5a: A) pre-crystallisation, B) midway through, and C) post-crystallisation.

In one sense then, the carbonate ions have "further" to rotate in forming (00.1). Indeed, it is easily shown that the average change in ϕ that each carbonate in ACC must undergo in forming a perfect (00.1) surface is around 57°, in contrast to only 18° for (01.2). A likely consequence is that the correct charge density (a significant driver of crystallisation) will take longer to emerge for (00.1) than for any other surface. This is because the ϕ-distribution determines the charge density that each carbonate layer exposes to its neighbouring layers (due to the charge distribution of the carbonate

ions).

The results from this study offer a possible explanation for the dominance of (01.2)-oriented crystallisation on self-assembled monolayers and other organic substrates [30, 31, 32]. For instance, in the case of carboxylate terminated alkyl thiols, self-assembled on gold substrates, the headgroup spacing is almost perfectly commensurate with the (00.1) surface of calcite and yet the (01.2) face crystallises [9, 30]. The higher growth rate of (01.2) observed in this study could be responsible, although in view of the disparity between our model and the experimental conditions on organic substrates, this is somewhat speculative.

4. Conclusions

The crystallisation of calcite from an ACC precursor within the confines of a cylindrical potential were simulated using molecular dynamics. The relative growth rates of six surfaces were measured and reported. The non-polar surfaces crystallised at a rate consistent with crystal growth models whereas the two polar surfaces were both unexpectedly slow, crystallising at a rate comparable to the slow-growing, low-energy (10.4) surface. This was especially true for (00.1).

An investigation of the structural evolution within the polar surfaces revealed that the charge separation (layering) occurred rapidly in the vicinity of the crystal surface and that the rate-limiting step for the crystal growth was the ionic ordering within those layers. We have proposed that growth in the [00.1] direction is inhibited as a consequence of the carbonate ions in ACC having further to rotate (with respect to the growth direction) than

they do for any other crystal orientation. This, in turn, could impede the emergence of the charge density displayed by each layer.

The results and analysis presented here offer insight into the observed crystallisation rates of calcium carbonate in molecular dynamics simulations.

Acknowledgements

This work was supported by the Engineering and Physical Sciences Research Council [grant number EP/I001514/1]. This Programme Grant funds the Materials Interface with Biology (MIB) consortium. RD acknowledges funding from EPSRC under the Molecular Modelling and Materials Science Industrial Doctorate Centre and from Pacific Northwestern National Laboratory.

[1] L. Gower, Biomimetic model systems for investigating the amorphous precursor pathway and its role in biomineralization, ChemInform 40 (5) (2009) no–no.

[2] S. Weiner, I. Sagi, L. Addadi, Choosing the crystallization path less traveled, Science 309 (5737) (2005) 1027–1028.

[3] Y. Politi, T. Arad, E. Klein, S. Weiner, L. Addadi, Sea urchin spine calcite forms via a transient amorphous calcium carbonate phase, Science 306 (5699) (2004) 1161–1164.

[4] Y. Gong, C. Killian, I. Olson, N. Appathurai, A. Amasino, M. Martin, L. Holt, F. Wilt, P. Gilbert, Phase transitions in biogenic amorphous calcium carbonate, Proceedings of the National Academy of Sciences 109 (16) (2012) 6088–6093.

[5] F. Meldrum, S. Hyde, Morphological influence of magnesium and organic additives on the precipitation of calcite, Journal of crystal growth 231 (4) (2001) 544–558.

[6] E. Loste, F. Meldrum, Control of calcium carbonate morphology by transformation of an amorphous precursor in a constrained volume, Chemical Communications (10) (2001) 901–902.

[7] E. Loste, R. Park, J. Warren, F. Meldrum, Precipitation of calcium carbonate in confinement, Advanced Functional Materials 14 (12) (2004) 1211–1220.

[8] Y. Kim, N. Hetherington, E. Noel, R. Kröger, J. Charnock, H. Christenson, F. Meldrum, Capillarity Creates Single-Crystal Calcite Nanowires from Amorphous Calcium Carbonate, Angewandte Chemie 123 (52) (2011) 12780–12785.

[9] D. Quigley, P. Rodger, C. Freeman, J. Harding, D. Duffy, Metadynamics simulations of calcite crystallization on self-assembled monolayers, The Journal of chemical physics 131 (2009) 094703.

[10] C. Freeman, J. Harding, D. Quigley, P. Rodger, Structural control of crystal nuclei by an eggshell protein, Angewandte Chemie International Edition 49 (30) (2010) 5135–5137.

[11] D. Quigley, C. Freeman, J. Harding, P. Rodger, Sampling the structure of calcium carbonate nanoparticles with metadynamics, The Journal of Chemical Physics 134 (2011) 044703.

[12] C. Stephens, S. Ladden, F. Meldrum, H. Christenson, Amorphous calcium carbonate is stabilized in confinement, Advanced Functional Materials 20 (13) (2010) 2108–2115.

[13] E. Beniash, L. Addadi, S. Weiner, Cellular control over spicule formation in sea urchin embryos: a structural approach, Journal of structural biology 125 (1) (1999) 50–62.

[14] Y. Politi, R. Metzler, M. Abrecht, B. Gilbert, F. Wilt, I. Sagi, L. Addadi, S. Weiner, P. Gilbert, Transformation mechanism of amorphous calcium carbonate into calcite in the sea urchin larval spicule, Proceedings of the National Academy of Sciences 105 (45) (2008) 17362–17366.

[15] S. Raz, P. Hamilton, F. Wilt, S. Weiner, L. Addadi, The transient phase of amorphous calcium carbonate in sea urchin larval spicules: the involvement of proteins and magnesium ions in its formation and stabilization, Advanced Functional Materials 13 (6) (2003) 480–486.

[16] B. Pichon, P. Bomans, P. Frederik, N. Sommerdijk, A quasi-time-resolved CryoTEM study of the nucleation of CaCO3 under langmuir monolayers, Journal of the American Chemical Society 130 (12) (2008) 4034–4040.

[17] E. Pouget, P. Bomans, J. Goos, P. Frederik, N. Sommerdijk, et al., The initial stages of template-controlled CaCO3 formation revealed by cryo-TEM, Science 323 (5920) (2009) 1455–1458.

[18] DL_POLY Classic code.
URL `http://www.ccp5.ac.uk/DL_POLY_CLASSIC`

[19] A. Pavese, M. Catti, G. Price, R. Jackson, Interatomic potentials for CaCO3 polymorphs (calcite and aragonite), fitted to elastic and vibrational data, Physics and chemistry of minerals 19 (2) (1992) 80–87.

[20] P. Steinhardt, D. Nelson, M. Ronchetti, Bond-orientational order in liquids and glasses, Physical Review B 28 (2) (1983) 784.

[21] W. Lechner, C. Dellago, Accurate determination of crystal structures based on averaged local bond order parameters, The Journal of chemical physics 129 (2008) 114707.

[22] D. Quigley, P. Rodger, Free energy and structure of calcium carbonate nanoparticles during early stages of crystallization, The Journal of chemical physics 128 (2008) 221101.

[23] G. Wulff, On the question of speed of growth and dissolution of crystal surfaces, Zeitschrift Fur Krystallographie Und Mineralogie 34 (5/6) (1901) 449–530.

[24] R. Docherty, G. Clydesdale, K. Roberts, P. Bennema, Application of Bravais-Friedel-Donnay-Harker, attachment energy and Ising models to predicting and understanding the morphology of molecular crystals, Journal of Physics D: Applied Physics 24 (1991) 89.

[25] A. Bravais, Etudes cristallographiques, Gauthier-Villars, 1866.

[26] J. Donnay, D. Harker, A new law of crystal morphology extending the law of Bravais, Am. Mineral 22 (5) (1937) 446–467.

[27] P. Hartman, P. Bennema, The attachment energy as a habit controlling factor: I. Theoretical considerations, Journal of Crystal Growth 49 (1) (1980) 145–156.

[28] N. de Leeuw, S. Parker, Surface structure and morphology of calcium carbonate polymorphs calcite, aragonite, and vaterite: An atomistic approach, The Journal of Physical Chemistry B 102 (16) (1998) 2914–2922.

[29] C. Freeman, Q. Hu, M. Nielsen, J. Tao, J. De Yoreo, J. Harding, Surface Selectivity of Calcite on Self-Assembled Monolayers. Forthcoming.

[30] A. Travaille, J. Donners, J. Gerritsen, N. Sommerdijk, R. Nolte, H. van Kempen, Aligned growth of calcite crystals on a self-assembled monolayer, Advanced Materials 14 (7) (2002) 492.

[31] D. Volkmer, M. Fricke, D. Vollhardt, S. Siegel, Crystallization of (012) oriented calcite single crystals underneath monolayers of tetra (carboxymethoxy) calix [4] arenes, J. Chem. Soc., Dalton Trans. (24) (2002) 4547–4554.

[32] A. Berman, D. Ahn, A. Lio, M. Salmeron, A. Reichert, D. Charych, Total alignment of calcite at acidic polydiacetylene films: cooperativity at the organic-inorganic interface, SCIENCE-NEW YORK THEN WASHINGTON- (1995) 515–515.

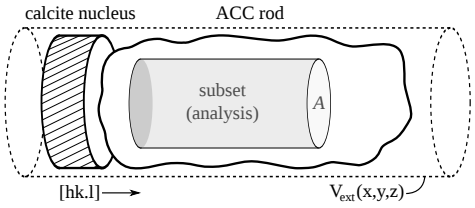

Figure 1: A schematic diagram of our atomistic model. A frozen calcite cylinder with an (hk.l) face induces crystallisation in an amorphous rod within the confines of a cylindrical potential. The subset is used in the analysis as described in §2.2.

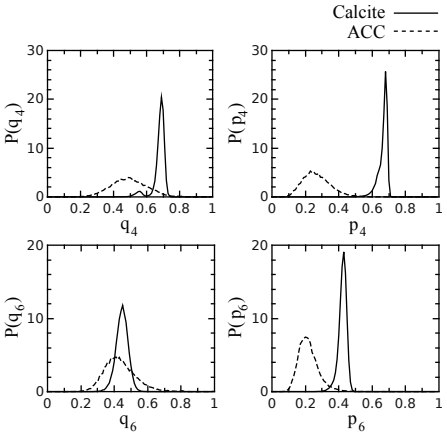

Figure 2: The distribution of a selection of local order parameters in bulk calcite (solid) and bulk ACC (dashed) at 1000 K and zero pressure. The calcium and carbonate ions are treated as indistinguishable particles.

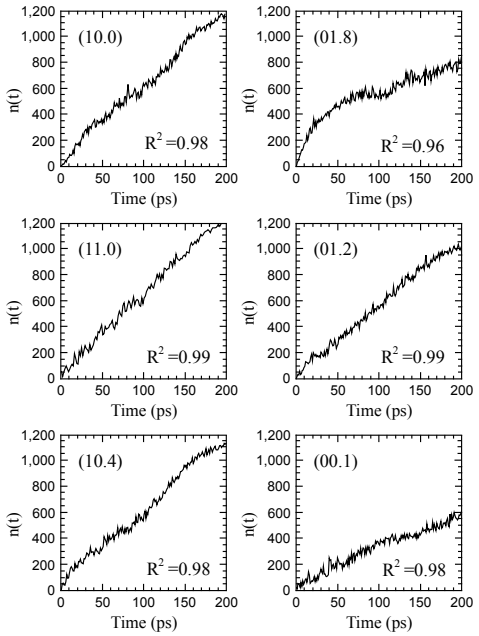

Figure 3: The function $n(t)$ for each rod during a 200 ps interval. This function counts the number of ions belonging to the calcite grain that fall within our subset. *For (01.8) the R^2 value corresponds only to the first 30 ps.

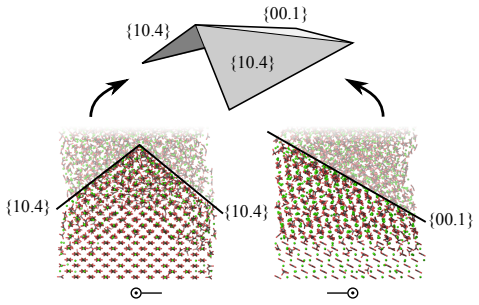

Figure 4: The growth surface in the (01.8) nanorod after 100 ps consisted of a pair of {10.4} planes and a {00.1} plane.

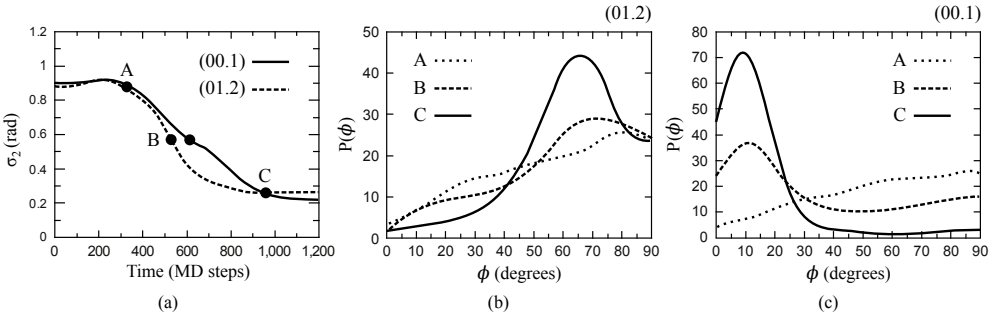

Figure 5: (a) The order within the second carbonate layer of the (00.1) and (01.2) nanorods as a function of time. The ionic ordering is evidently impeded in (00.1). The (smoothed) distribution of ϕ at the three labelled points (A, B, and C) are shown for (01.2) in (b) and (00.1) in (c).

Surface	Sample	G (relative)	ρ (ions/nm^2)	E_{attach} (kJ/mol) [28]
(10.0)		1.82	4.6	-760
(01.8)		1.65	6.3	-
(11.0)		1.44	8.1	-291
(01.2)		1.19	6.3	-
(10.4)		1.06	9.9	-75
(00.1)		1.00	4.5	-334 (Ca)

Table 1: The six orientations investigated in this work, ordered based on the growth rates G. The ionic densities ρ and attachment energies E_{attach} (where available) are also specified. The ionic colours in the samples correspond to Ca (green), C (grey), and O (red).